Experimental Mechanics (2017) 57:313–324
DOI 10.1007/s11340-016-0215-5

Measurement of Elastic Properties of Epoxy Molding Compound by Single Cylindrical Configuration with Embedded Fiber Bragg Grating Sensor

Y. Sun[1] · H.-S. Lee[1] · B. Han[1]

Received: 20 March 2016 / Accepted: 16 September 2016 / Published online: 18 October 2016
© Society for Experimental Mechanics 2016

Abstract We propose a novel experimental method, based on a fiber Bragg grating (FBG) sensor, to measure the elastic properties of epoxy molding compound (EMC) from a single specimen configuration. The FBG sensor is embedded in the center of a cylindrical EMC specimen, and deforms together with the EMC. The Bragg wavelength (BW) shifts are documented during compressive and hydrostatic loadings. Young's modulus and bulk modulus are determined from the BW shifts using the relationships between the elastic constants and the BW shift. Two major developments to accommodate the unique requirements of EMC testing include: (1) a large mechanical pressure to be applied during curing; and (2) a very high gas pressure required for hydrostatic testing. The shear modulus and Poisson's ratio are calculated from the two measured constants to provide a complete set of elastic properties of EMC.

Keywords Epoxy molding compound · Fiber Bragg grating · Hydrostatic pressure · Young's modulus · Bulk modulus · Poisson's ratio · Shear modulus

Introduction

Epoxy molding compounds (EMCs) are thermosetting polymers filled with a large quantity of silica particles. They have been widely used to protect active devices in semiconductor packaging. In the manufacturing process, EMCs are converted to a highly viscous liquid form by heat and then injected into a mold by applying a pressure.

The warpage and residual stresses, caused by the mismatch of the coefficient of thermal expansion (CTE) between EMC and adjacent materials, are two most important mechanical quantities in assessing reliability of semiconductor packaging components. The warpage of the components can cause an "opening" or "short" of interconnections between the components and the motherboard. Excessive residual stresses can cause delamination and even chip cracking [1, 2]. Temperature-dependent mechanical properties are crucial for the accurate prediction of the thermo-mechanical behavior of semiconductor packages encapsulated by EMCs.

The elastic properties of the material have the following relationships [3]:

$$K = \frac{EG}{9G-3E} \quad , \quad G = \frac{E}{2(1+\nu)} \tag{1}$$

where E, G and K are the Young's modulus, shear modulus and bulk modulus, respectively; and ν is the Poisson's ratio. At least two of the four constants have to be measured experimentally for thermo-mechanical modeling.

There were several attempts to measure the two required properties. In Ref. [3], Young's modulus and Poisson's ratio were measured by strain gauges. The measurement was simple but the measured data contained some uncertainties caused by the undesired reinforcement of the strain gauge, especially at high temperatures where the modulus was relatively low.

A full-field displacement measurement technique called moiré interferometry was employed to measure the axial and transverse strains simultaneously [4], from which the Young's modulus and Poisson's ratio were determined. The method

✉ B. Han (SEM fellow)
bthan@umd.edu

[1] Department of Mechanical Engineering, University of Maryland, College Park, MD 20742, USA

provides high accuracy, but its practice has been limited due to the complexity of the optical system and other stringent requirements, such as a high frequency diffraction grating, a vibration-free loading condition, etc.

The frequency-temperature sweep of a dynamic mechanical analyzer (DMA) was implemented to measure the temperature dependent modulus [5]. This technique can be routinely practiced using commercial equipment, but it is usually difficult to fabricate coupons to obtain all elastic constants other than the Young's modulus. A comprehensive study about the time and temperature-dependent Poisson's ratio of viscoelastic materials is presented in Ref.[6].

The bulk modulus of polymers was measured in the past by a dilatometer [7, 8] using a fluid pressure. The volume change of the polymer was monitored as a function of time after the pressure was applied, and the bulk compliance of the polymer was determined from the volume change. As mentioned in Ref. [8], when working at temperatures above T_g, the weight of a rod added undesired additional creep loading to the specimen, which caused an underestimation of the true volume change.

The Fiber Bragg Grating (FBG) sensor has been proven an effective method to characterize the thermo-mechanical properties of polymers [9–13]. In this method, an FBG is embedded at the center of a cylindrical specimen, and deforms together with the specimen. The properties are determined from the Bragg wavelength (BW) shift using the relationship based on the generalized plane strain condition [9, 13].

In this paper, a novel experimental method, based on the fiber Bragg grating (FBG) sensor, is proposed and implemented to measure the elastic properties of EMC materials from a single specimen configuration. Two major developments to accommodate the unique requirements of EMC testing include: (1) a large mechanical pressure (7 MPa) to be applied during curing; and (2) a very high gas pressure (10 MPa) required for hydrostatic testing. A new governing equation for a general loading is presented first. The two developments are described in detail and the results obtained from advanced EMC materials are presented.

Governing Equations

The proposed method utilizes the basic characteristic of the fiber Bragg grating (FBG). As illustrated in Fig. 1, the FBG is embedded in a cylindrical specimen, and deforms together with the specimen. The Bragg wavelength (BW) change is documented during testing, and the mechanical properties of the specimen are determined inversely from the relationship between the elastic constants and the BW shift. A closed form solution of an annular substrate encasing a circular fiber (axisymmetric problem) under the generalized plane strain condition provides the relationship.

Let us consider the assembly subjected to an axial pressure, P_1, and a radial pressure, P_2 (Fig. 1). The stress distribution of the fiber and polymer can be expressed as:

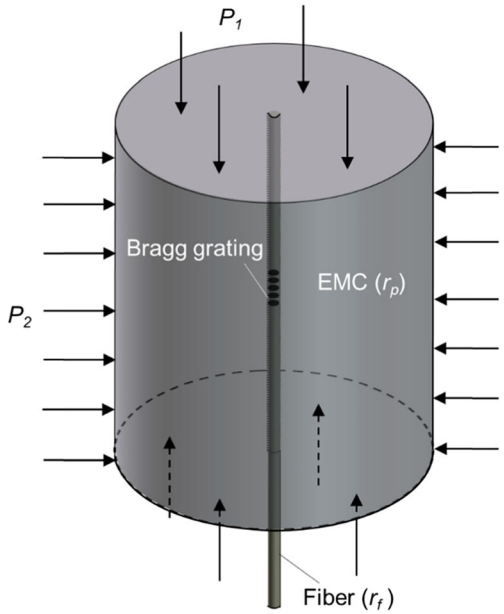

Fig. 1 Loading condition

$$
\begin{aligned}
\sigma_{rr}(r) &= \frac{E_f}{1+\nu_f}\left[\frac{C_{1f}}{1-2\nu_f} - \frac{C_{2f}}{r^2}\right] + \frac{E_f\nu_f c}{(1+\nu_f)(1-2\nu_f)}, \quad 0 \le r \le r_f \\
\sigma_{\theta\theta}(r) &= \frac{E_f}{1+\nu_f}\left[\frac{C_{1f}}{1-2\nu_f} + \frac{C_{2f}}{r^2}\right] + \frac{E_f\nu_f c}{(1+\nu_f)(1-2\nu_f)}, \quad 0 \le r < r_f \\
\sigma_{zz}(r) &= \frac{2E_f\nu_f C_{1f}}{(1+\nu_f)(1-2\nu_f)} + \frac{2E_f{\nu_f}^2 c}{(1+\nu_f)(1-2\nu_f)} + E_f c, \quad 0 \le r < r_f \\
u(r) &= C_{1f} r + \frac{C_{2f}}{r}, \quad 0 \le r \le r_f \\
\sigma_{rr}(r) &= \frac{E_p}{1+\nu_p}\left[\frac{C_{1p}}{1-2\nu_p} - \frac{C_{2p}}{r^2}\right] + \frac{E_p\nu_p c}{(1+\nu_p)(1-2\nu_p)}, \quad r_f \le r \le r_p \\
\sigma_{\theta\theta}(r) &= \frac{E_p}{1+\nu_p}\left[\frac{C_{1p}}{1-2\nu_p} + \frac{C_{2p}}{r^2}\right] + \frac{E_p\nu_p c}{(1+\nu_p)(1-2\nu_p)}, \quad r_f < r \le r_p \\
\sigma_{zz}(r) &= \frac{2E_p\nu_p C_{1p}}{(1+\nu_p)(1-2\nu_p)} + \frac{2E_p{\nu_p}^2 c}{(1+\nu_p)(1-2\nu_p)} + E_p c, \quad r_f \le r \le r_p \\
u(r) &= C_{1p} r + \frac{C_{2p}}{r}, \quad r_f \le r \le r_p
\end{aligned}
\tag{2}
$$

where σ_{zz}, σ_{rr} and $\sigma_{\theta\theta}$ are the axial, radial and hoop stress components, respectively; E, ν and r are the Young's modulus, Poisson's ratio and radius, where the subscripts, f and p denote the fiber and polymer; $u(r)$ is the radial displacement; the coefficients C_{1p}, C_{2p}, C_{1f}, C_{2f} and c are the unknown constants that can be determined from the boundary conditions.

Applying the following boundary conditions,

$$
\begin{aligned}
&u(0) = 0 \\
&u_f(r_f) = u_p(r_f) \\
&\sigma_{rr}^p(r_p) = P_2 \\
&\sigma_{rr}^p(r_f) = \sigma_{rr}^f(r_f) \\
&\frac{\int_0^b 2\sigma_{zz}(r) r \mathrm{d}r}{{r_p}^2} = P_1
\end{aligned}
\tag{3}
$$

the coefficients in Eq. (2) can be calculated as:

$$
\begin{aligned}
C_{1p} &= \frac{CE-BF}{AE-BD} \\
c &= \frac{CD-AF}{BD-AE} \\
C_{2p} &= \left(\frac{C_{1p}}{(1-2\nu_p)(1+\nu_p)} + \frac{\nu_p c}{(1-2\nu_p)(1+\nu_p)} - \frac{P_1}{E_p}\right)(1+\nu_p){r_p}^2 \\
C_{1f} &= C_{1p} + \frac{C_{2p}}{{r_p}^2} \\
C_{2f} &= 0
\end{aligned}
\tag{4}
$$

where

$$
\begin{aligned}
A &= \frac{E_p}{(1+\nu_p)(1-2\nu_p)}\left(\frac{{r_p}^2}{{r_f}^2}-1\right) + \frac{E_f}{(1+\nu_f)(1-2\nu_f)}\left(1+\frac{{r_p}^2}{{r_f}^2(1-2\nu_p)}\right) \\
B &= \frac{E_p\nu_p}{(1+\nu_p)(1-2\nu_p)}\left(\frac{{r_p}^2}{{r_f}^2}-1\right) + \frac{E_f\nu_f}{(1+\nu_f)(1-2\nu_f)}\left(1+\frac{{r_p}^2}{{r_f}^2(1-2\nu_p)}\frac{\nu_p}{\nu_f}\right) \\
C &= \left(1+\frac{E_f}{(1+\nu_f)(1-2\nu_f)}\frac{(1+\nu_p)}{E_p}\right)\frac{{r_p}^2}{{r_f}^2}P_2 \\
D &= \frac{2E_p\nu_p}{(1+\nu_p)(1-2\nu_p)}\left(\frac{{r_p}^2}{{r_f}^2}-1\right) + \frac{2E_f\nu_f}{(1+\nu_f)(1-2\nu_f)}\left(1+\frac{{r_p}^2}{{r_f}^2(1-2\nu_p)}\right) \\
E &= \frac{2E_p{\nu_p}^2}{(1+\nu_p)(1-2\nu_p)}\left(\frac{{r_p}^2}{{r_f}^2}-1\right) + \frac{2E_f\nu_f}{(1+\nu_f)(1-2\nu_f)}\left(\nu_f+\frac{\nu_p{r_p}^2}{{r_f}^2(1-2\nu_p)}\right) \\
&\quad + E_f + E_p\left(\frac{{r_p}^2}{{r_f}^2}-1\right) \\
F &= \frac{2E_f\nu_f}{(1+\nu_f)(1-2\nu_f)E_p}(1+\nu_p)\frac{{r_p}^2}{{r_f}^2}P_2 + \frac{{r_p}^2}{{r_f}^2}P_1
\end{aligned}
\tag{5}
$$

The above closed-form solution was verified by a 2-D axisymmetric finite element model. The length of the assembly was 15 mm, and the radius of the polymer and the fiber were 4.4 mm and 62.5 μm, respectively. The properties of the materials used in the modeling were: $E_f = 73$ GPa, $\nu_f = 0.17$, $E_p = 10$ GPa, and $\nu_p = 0.35$. The applied pressure was $\frac{P_1}{2} = P_2 = P$. The boundary conditions of the model were identical to those shown in Fig. 1. The radial stresses normalized by the applied pressure are compared in Fig. 2. The results confirm the accuracy of the analytical solution.

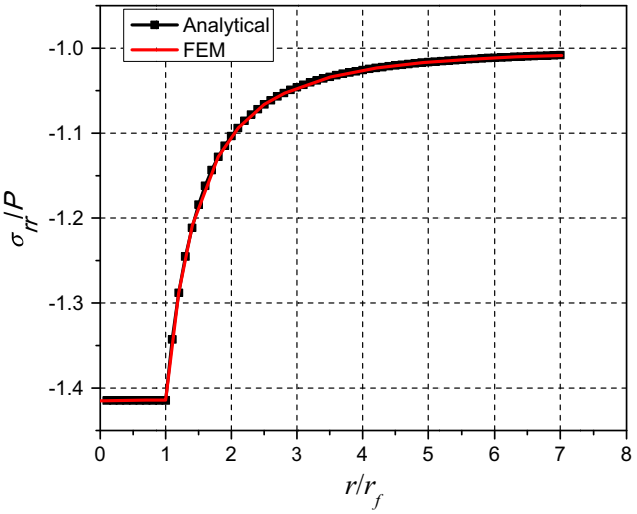

Fig. 2 Comparison of the analytical solution with the numerical solution

The embedded FBG serves as a strain sensor. The Bragg wavelength (BW) shift occurs when the FBG is subjected to stresses. The relationship between the BW shift and the stress can be expressed as [9]:

$$
\Delta\lambda = \frac{1}{E_f}\left\{\left[1-\frac{n^2}{2}\left(P_{12}-(P_{12}+P_{11})\nu_f\right)\right]\sigma_{zz}^f - \left[2\nu_f + \frac{n^2}{2}\left((1-\nu_f)P_{11} + (1-3\nu_f)P_{12}\right)\right]\sigma_{rr}^f\right\}\lambda_i \tag{6}
$$

where $\Delta\lambda$ is the BW shift, λ_i is the initial BW, n is the effective refractive index, and P_{ij} are strain optic constants [14, 15].

By substituting Eqs. (1) and (2) into (6), the BW shift can take the following form:

$$
\Delta\lambda = \Pi\left(E_p, \nu_p, \beta\right) \tag{7}
$$

where $\beta = \frac{r_p}{r_f}$ (will be referred to as "configuration"); E_p and ν_p are the Young's modulus and Poisson's ratio of the polymer; and Π is a nonlinear function that can be expressed explicitly. More detailed procedures to obtain Eq. (7) are shown in Appendix.

For a given configuration, β, the BW shift is a function of any two of four elastic constants of the polymer (Eqs. (1) and (7)). The two constants can be inversely determined from the BW shifts measured from two independent experiments. Although theoretically possible, determining two unknown parameters from an extremely non-linear equation can be very tricky. A special case arises for uniaxial loading, where the effect of the polymer's Poisson's ratio becomes insignificant. The following analysis provides a procedure to determine the two required constants *sequentially* from two sets of experimental data.

Uniaxial Loading

The loading condition for uniaxial compression is $P_1 \neq 0$; $P_2 = 0$. The effect of Poisson's ratio under this loading

condition is analyzed numerically using the same axisymmetric model and the result is shown in Fig. 3. The plot shows the BW shifts as a function of configuration, where three Poisson's ratios (0.2, 0.3, 0.45) and three moduli (0.1 GPa, 0.5 GPa, 2.5 GPa) are considered. For each modulus, the applied stress is adjusted to produce the same BW shift for $\beta = 20$. The plot clearly indicates that, for the same modulus, the ΔBW is only a function of configuration; it remains the same regardless of the Poisson's ratios. Thus, by assuming a typical value for Poisson's ratio (e.g., 0.3), the Young's modulus can be determined from the BW shifts obtained from a uniaxial compression test by:

$$E_p = \Pi^{-1}\left(\Delta\lambda, \beta, \nu_p = 0.3\right) \tag{8}$$

Hydrostatic Loading

The loading condition of hydrostatic testing is $P_1 = P_2 \neq 0$. As mentioned earlier, the BW shift for a given configuration can be expressed in terms of any two elastic constants. With Young's modulus obtained from the compressive test, the bulk modulus can be determined from the BW shifts obtained from a hydrostatic test using:

$$K_p = \Pi^{-1}\left(\Delta\lambda, \beta, E_p = \text{ constant}\right) \tag{9}$$

where K_p is the bulk modulus of the polymer. The form of the inverse function is the same as the uniaxial case, but the initial input values are different.

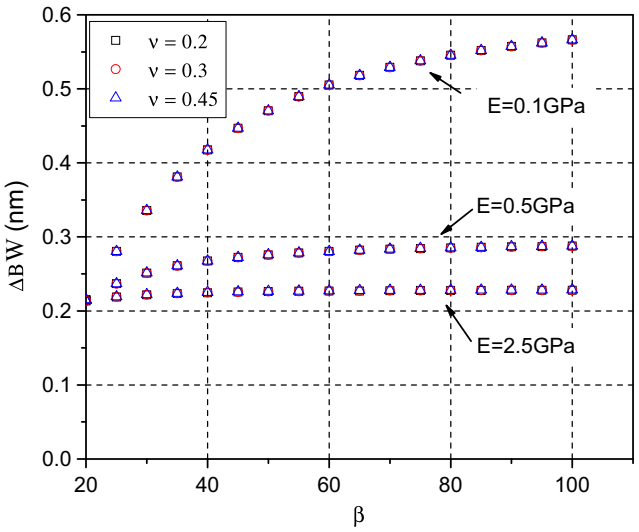

Fig. 3 BW shifts as a function of configuration

Experiment

Fabrication of an EMC specimen requires a custom-designed mold that maintains the optical fiber at the center of the mold while curing EMC under a high pressure. The required high pressure is achieved by a mechanical plunger driven by an air cylinder. The air cylinder based apparatus is modified to conduct uniaxial compression testing. A special apparatus utilizing pressurized He gas is also developed to provide the much higher pressure required for hydrostatic testing. This section describes the test apparatuses and procedures.

Specimen Fabrication

The stainless-steel mold assembly to fabricate the specimens is shown in Fig. 4a. The assembly consists of a bottom mold, a

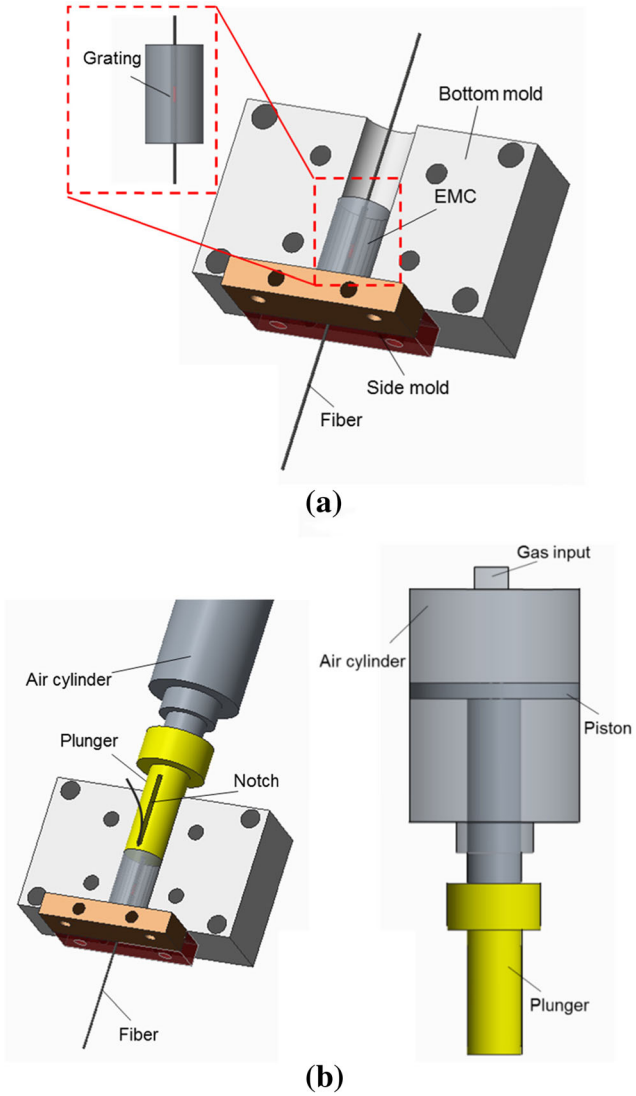

Fig. 4 Mold assembly to fabricate the specimen: **a** mold and pellet and **b** plunger and air cylinder

symmetric top mold (not shown in the figure) and two side molds. The uncured EMC pellet sits in the cylindrical chamber of the mold, whose diameter is 8.8 mm.

A small through hole was drilled in the center of the EMC pellet. The optical fiber (diameter of 125 μm) was carefully inserted through the hole (see the insert of Fig. 4a). The fiber position was adjusted until the Bragg grating (5 mm long) was placed in the middle of pellet; this was achieved by making a mark on the fiber considering the length of the mold.

A mechanical plunger was also mounted on the mold and was in direct contact with the pellet (Fig. 4b). A small notch and a small through-hole (not shown) were machined on the side and the bottom of the plunger, respectively. The fiber went through the hole and the notch allowed the fiber to go out of the plunger; the fiber was pulled to have a small amount of tension during curing to maintain its straightness. As shown in Fig. 4(b), the plunger was mechanically connected to the piston of an air cylinder (SR121: BIMBA) to apply the pressure to the specimen during curing.

The complete system is shown in Fig. 5. The mold (with the pellet) was mounted on a high precision hot/cold plate (HCP304: Instec), which provided temperature control with a resolution of ±0.05 °C. The compressed air line was connected to the pressure regulator (ER3000: Tescom), which was controlled by a PC to produce a desired air pressure to the air cylinder. The bottom end of the fiber was connected to the interrogator (sm125: Micro Optics) and the interrogator was connected to the PC to collect data from the FBG sensor.

The schematic illustration of the assembly after pre-processing is shown in Fig. 6. The internal surfaces of the mold were treated with a release agent and the pellet was wrapped with a very thin Teflon tape before the curing process started. This pre-processing ensured (1) no constraint from the mold walls (i.e., virtually zero-friction between the mold and the EMC) and (2) easy separation after curing. A rubber gasket was also placed between the plunger head and the specimen to eliminate the leakage during curing, especially after the high pressure was applied.

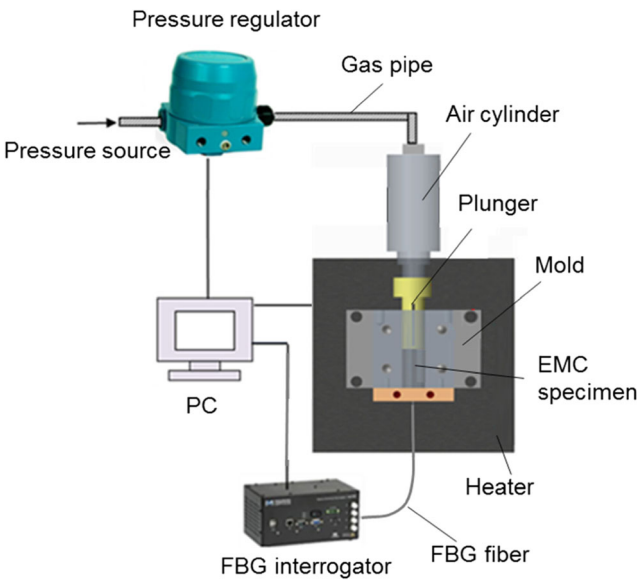

Fig. 5 Setup for specimen fabrication

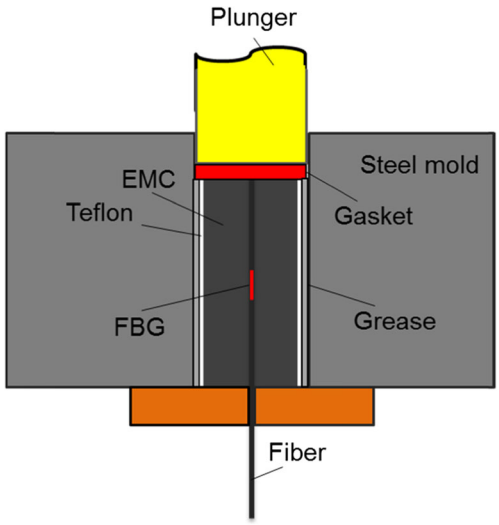

Fig. 6 Schematic illustration of specimen assembly after pre-processing

After the specimen temperature reached the curing temperature (175 °C), the required EMC curing pressure of 7 MPa was applied and maintained during curing. The maximum pressure of the compressed air line was only P_{source} = 0.69 MPa. The required mechanical pressure was achieved by the air cylinder whose piston diameter was much larger than the diameter of the plunger (see Fig. 4b).

The diameter of the piston that can produce the required pressure at P_{source} can be determined as

$$D_{piston} = \sqrt{\frac{P_{curing}}{P_{source}}} \times D_{plunger} = \sqrt{\frac{7\ \text{MPa}}{0.69\ \text{MPa}}} \times 8.8\ \text{mm} = 28.0\ \text{mm} \quad (10)$$

The air cylinder with D_{piston} = 31.75 mm (1.25 inch) was selected for the system. The air pressure to produce P_{curing} was then determined as:

$$P_{source} = \left(\frac{D_{plunger}}{D_{piston}}\right)^2 \times P_{curing} = \left(\frac{8.8\ \text{mm}}{31.75\ \text{mm}}\right)^2 \times 7\ \text{MPa} = 0.54\ \text{MPa}\ (78\ \text{psi}) \quad (11)$$

The specimen was released from the mold after curing it for 5 minutes and was subsequently subjected to a post-mold curing process (for 2 hours at the curing temperature) to ensure complete curing. The cured specimen is shown in Fig. 7.

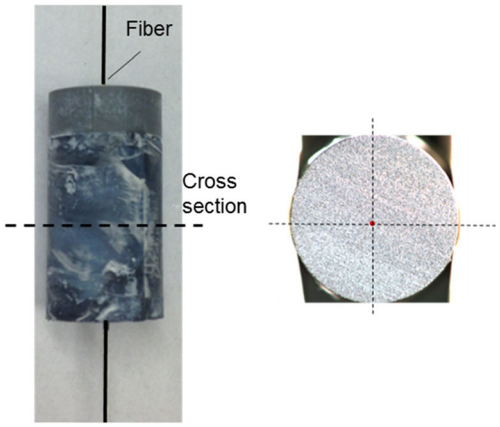

Fig. 7 Cured EMC specimen and its cross section

The diameter and the length of the cured EMC was 8.8 mm and 15 mm.

The location and the straightness of the Bragg grating are very important to obtain a correct signal from the specimen. It was achieved by marking the relative position of the Bragg grating and gently pulling the fiber during the initial stage of curing. The cross-section of the cured specimen was examined to confirm the fiber location. The cross section image of the specimen is shown in Fig. 7. The result confirmed that the fiber position was maintained at the center of the specimen after curing. The straightness was also verified by several cross-sections made along different positions.

Uniaxial Testing

The setup used to prepare the specimen was slightly modified to measure temperature-dependent Young's modulus. The set-up was identical to the setup shown in Fig. 4 except that the diameter of the cylindrical chamber was slightly larger than the diameter of the specimen allowing the specimen to deform freely in the radial direction during compressive loading. The setup was mounted on the same heating stage shown in Fig. 5.

Hydrostatic Testing

Hydrostatic testing required a pressure much higher than the pressure used in the curing setup. A small test chamber was designed to accommodate a high gas pressure for hydrostatic testing (Fig. 8). The chamber was fabricated from stainless steel for tight tolerance required for sealing. The specimen was placed freely inside the chamber. The fiber passed through a small hole on the bottom side of the chamber. The hole was also sealed by a thin layer of Teflon tape after placing the fiber. The chamber was mounted on the same heating stage shown in Fig. 5. The top of the chamber was connected to the gas pipe.

The required pressure was provided by a custom-designed high pressure system, illustrated schematically in Fig. 9. The

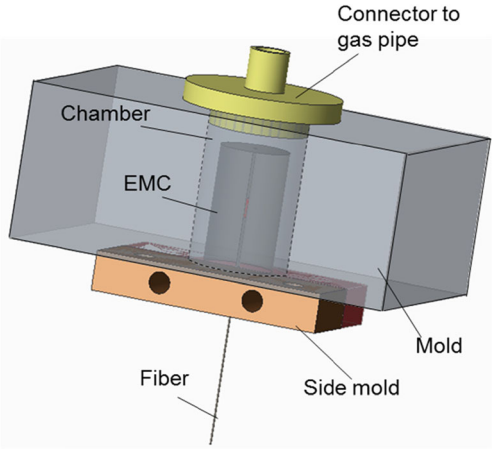

Fig. 8 Chamber for hydrostatic test

Helium tank provided a gas pressure of approximately 15.2 MPa. The output gas from the tank passed through the main regulator (26–2015: Tescom). The main regulator was controlled by a pilot controller (ER3000: Tescom) with a transducer (100–1500: Tescom) that provided the feedback to the computer. The controller was connected to a PC, which controlled and recorded the pressure. The output pressure to the test chamber was controlled with the accuracy of around 6.9 KPa and the target pressure was reached within 1 s. The maximum pressure output to the test chamber was 10.3 MPa.

It is to be noted that the heat can be generated immediately after the target pressure is applied to the test chamber since the gas present (i.e., air) in the chamber is suddenly compressed. The amount of heat generation can be estimated by [16]:

$$Q = \frac{5}{2} P_i V \left(\left(\frac{P_a}{P_i} \right)^{\frac{2}{7}} - 1 \right) \tag{12}$$

where Q is the heat generation in Joule, P_i and P_a are the initial and applied pressure in MPa, and V is the volume of the gas

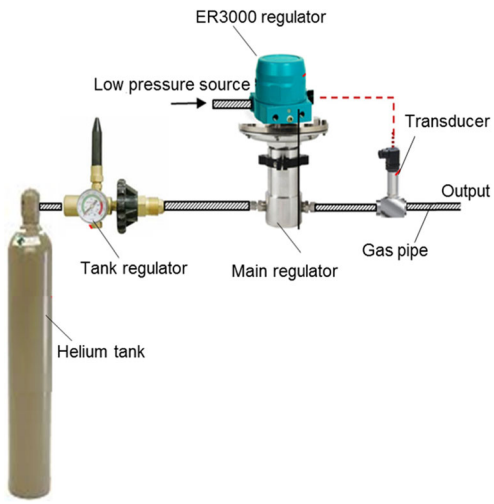

Fig. 9 High pressure system used for hydrostatic testing

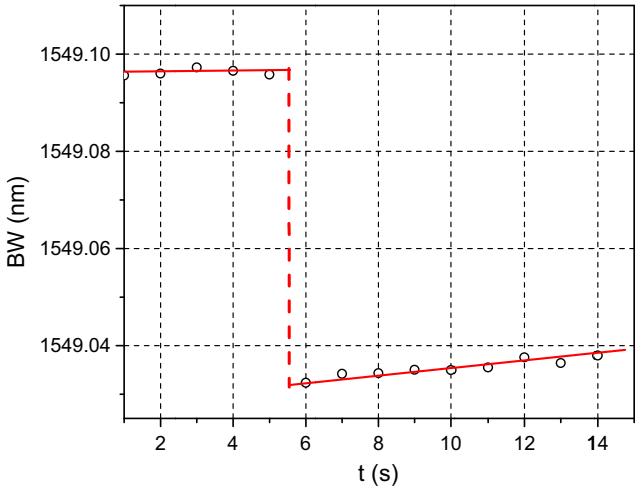

Fig. 10 BW before and after the hydrostatic pressure is applied

inside the chamber in mm^3 (i.e., the chamber volume – the specimen volume).

This undesired heat causes thermal expansion of the specimen, which offsets the hydrostatic strain of the specimen. The results obtained from the initial design of the chamber are shown in Fig. 10, which shows the BW as a function of time. The temperature was first maintained at a constant value and the hydrostatic pressure of 3.5 MPa was applied suddenly (≈5 s). The BW continued to increase after its sudden drop produced by the hydrostatic pressure. This gradual increase of the BW was caused by the thermal expansion of the specimen.

In practice, the thermal strain caused by $\Delta T < 0.1$ °C (within 1 micro-strain) is negligible compared to the hydrostatic strain (typically more than 100 micro-strain). Considering the specific heat (≈1 J/gK) and the thermal conductivity (≈1 W/mK) of the EMC [17], the heat generation should be smaller than 0.5 J. Using Eq. (12), the corresponding air volume was determined to be 1000 mm^3 at the maximum pressure of 10.5 MPa. The internal volume of the final chamber was around 1800 mm^3 and the volume of the specimen was 910 mm^3; the net air volume was 890 mm^3. The effect of the heat generation was virtually negated.

Results and Analysis

The temperature dependent Young's modulus is determined first from the uniaxial test data and the bulk modulus is subsequently determined from the hydrostatic test data.

Experiment Data

The EMC specimen was tested from 25 °C to 235 °C with a constant interval of 20 °C (at every 5 °C around the glass transition temperature). The mold was heated to the target temperature first. The BW increased with the temperature due to the thermal expansion of the EMC as well as the intrinsic thermal expansion of the fiber. The BW was monitored until it was stabilized, which confirmed the uniform temperature. A pre-determined pressure was applied and the BW change was recorded.

Another important practical aspect to be considered was the strong temperature-dependent modulus. Considering the resolution of the FBG interrogator about 1 pm, the ΔBW should be at least 100 pm to maintain the measurement uncertainty within 1 %. For this reason, three different stresses of 4.98 MPa, 1.8 MPa and 0.18 MPa were applied for the temperatures below, near and above the glass transition temperature, respectively; the corresponding air cylinder pressures were 344.7 KPa, 137.9 KPa, 13.8 KPa.

The BW change (ΔBW) was documented for 100 seconds after the pressure was applied. The representative data obtained from compressive testing at 25 °C, 125 °C and 175 °C are shown in Fig. 11, where the BW change (ΔBW) is normalized by the applied pressure. The constant BW before loading confirms the temperature stability of the specimen achieved during testing. It is worth noting that the stabilized BW increased with the temperature, which was caused by the temperature–dependent intrinsic property of FBG. The spectral response was also recorded and examined to ensure no spectral distortion during the loading.

It should be noted that, at temperatures 25 °C and 175 °C, which were below and above glass transition temperature, respectively, the BW remained constant after the pressure was applied, which indicated that the modulus was virtually time-independent. At 125 °C, which lies within the glass transition range, however, the BW continued to decrease after the pressure was applied due to the time-dependent behavior of the EMC near the glass transition temperature.

The same specimen was subjected to hydrostatic pressure. The representative data obtained at 25 °C, 125 °C and 175 °C are shown in Fig. 12. Three different pressures of 6.9 MPa, 5.5 MPa and 1.4 MPa were applied for the temperatures below, near and above the glass transition temperature, respectively. As expected, a similar time-dependent behavior was observed.

The material shows strong viscoelastic behavior in the glass transition range. The temperature-dependent modulus of the material is defined at a certain time (e.g., 1 s, 10s [18]), which is known as the "isochronous modulus." The temperature-dependent isochronous Young's modulus at 1 s was calculated first using Eq. (8). After the Young's modulus was determined, the bulk modulus was calculated using Eq. (9).

The results are shown in Fig. 13. The temperature-dependent properties measured at 1 s demonstrated a stiffness change of the material as a function of temperature. The glass

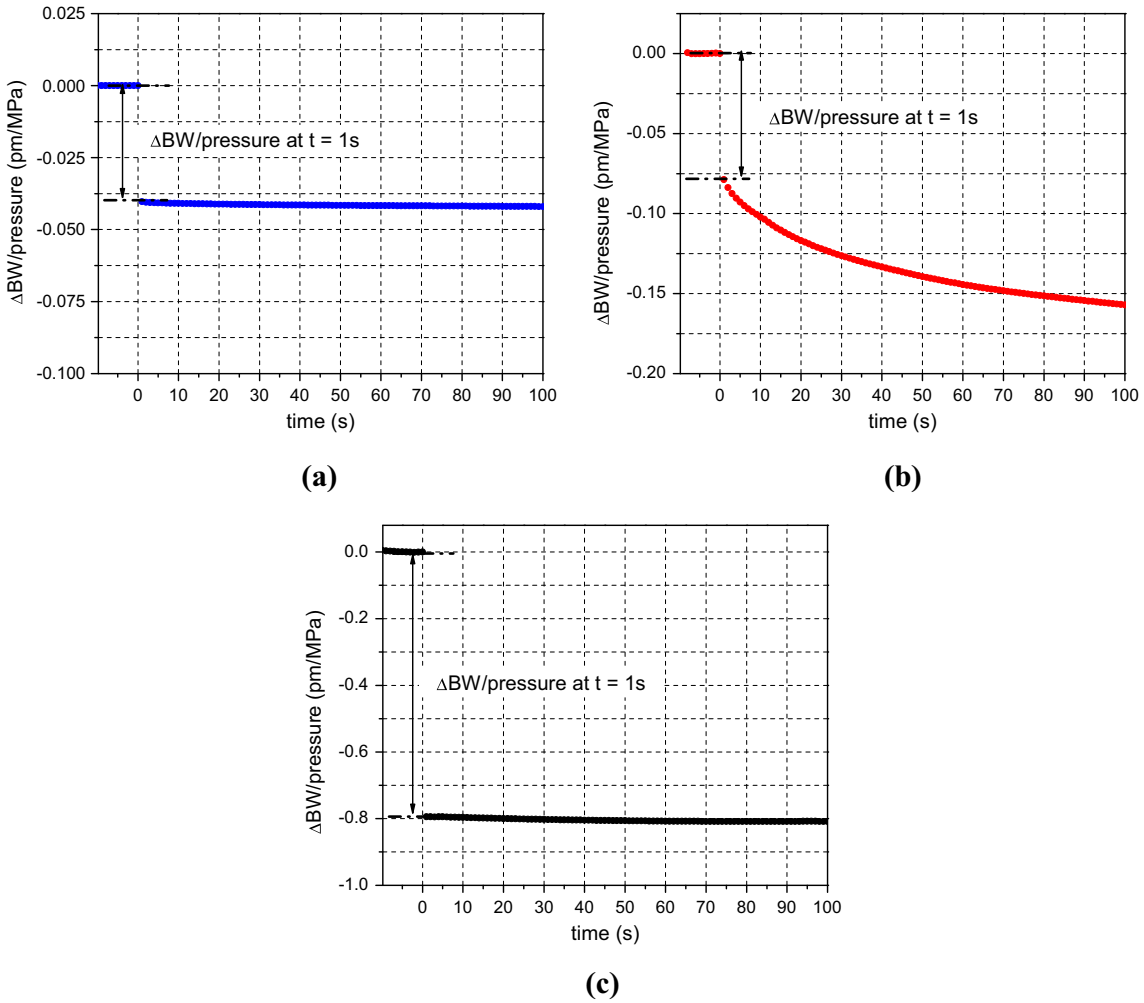

Fig. 11 BW changes normalized by the applied compressive pressure at **a** 25 °C, **b** 125 °C and **c** 175 °C

transition range of the material was around 110 °C to 140 °C shown in the figure. As expected, both moduli decreased rapidly over the glass transition region and became stabilized after the glass transition region.

The shear modulus and Poisson's ratio at 1 s were calculated from the two moduli using Eq. (1). All four temperature-dependent properties are also shown in Fig. 13. All three isochronous moduli decrease with the temperature while Poisson's ratio increases with the temperature. The Young's modulus is larger than the bulk modulus before T_g but it becomes smaller after T_g. It is caused by a much larger Poisson's ratio after T_g (0.43 after T_g compared to 0.21 before T_g). As expected, the shear modulus is always smaller than the Young's modulus and the bulk modulus. The Poisson's ratio increases as a function of temperature. It is worth noting that there have been discussions about the validity of Eq. (1) in the viscoelastic regime [6]; more experimental measurements are warranted to verify an applicable domain of Eq. (1).

Time-Dependent Properties in the Glass Transition Range

As mentioned earlier, the EMC material shows significant viscoelastic behavior in the glass transition range. The method proposed in this paper was implemented to measure the time-dependent properties in the glass transition range.

It should be noted that Eqs. (1)–(5) were derived from the elastic solution. It is routinely practiced that the elastic constants can be replaced by the corresponding time-dependent relaxation moduli or creep compliances. The accuracy of this approximation has been confirmed by the results reported in the literature [19, 20].

The time-dependent properties were determined at three temperatures within the glass transient range (115 °C, 125 °C, and 130 °C). The Young's modulus and bulk modulus were calculated first by replacing the elastic constant with the time dependent properties in Eqs. (8) and (9). Then, the corresponding shear modulus and Poisson's ratio were determined from the two properties.

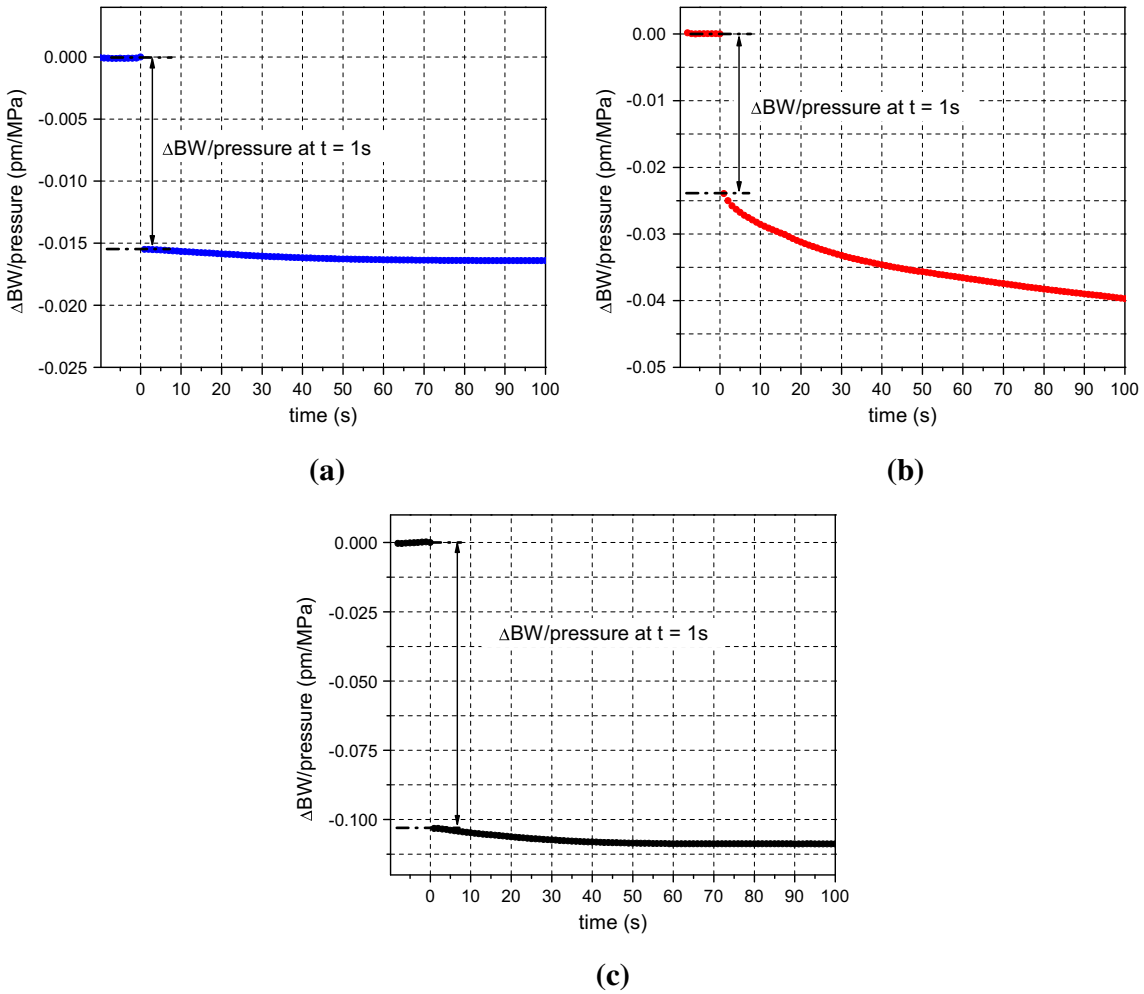

Fig. 12 BW change normalized by applied hydrostatic pressure at **a** 25 °C, **b** 125 °C and **c** 175 °C

The results are shown in Fig. 14. EMC consists of thermo-setting polymer and silica particles. As expected, the modulus decreases as a function of time while the Poisson's ratio increase. The viscoelastic behavior is quite different when the temperature is different by only 5 °C since all three temperatures lied in the glass transition temperature.

Discussion: Measurement Uncertainties

The gas pressure was directly applied to the specimen during hydrostatic testing. Thus, there was no load-transfer train, and the measurement uncertainties would be associated only with the accuracy of the pressure regulator. The output accuracy was around 6.9 KPa and its effect on the bulk modulus was negligible.

On the other hand, a mechanical plunger was used in uniaxial compression testing. The plunger was connected to a piston of an air cylinder. The friction of the load-train was unavoidable, especially, against the piston movement inside the cylinder. Furthermore, the applied pressure of the uniaxial testing was much smaller compared to the hydrostatic testing.

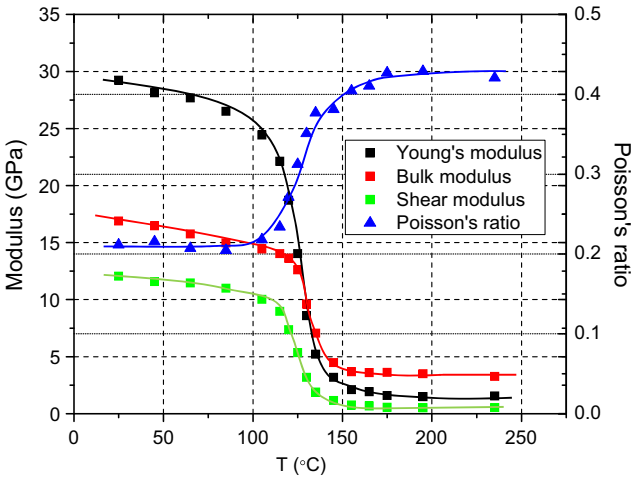

Fig. 13 Temperature dependent isochronous properties at t = 1 s, where shear modulus and Poisson's ratio were calculated from Young's modulus and bulk modulus

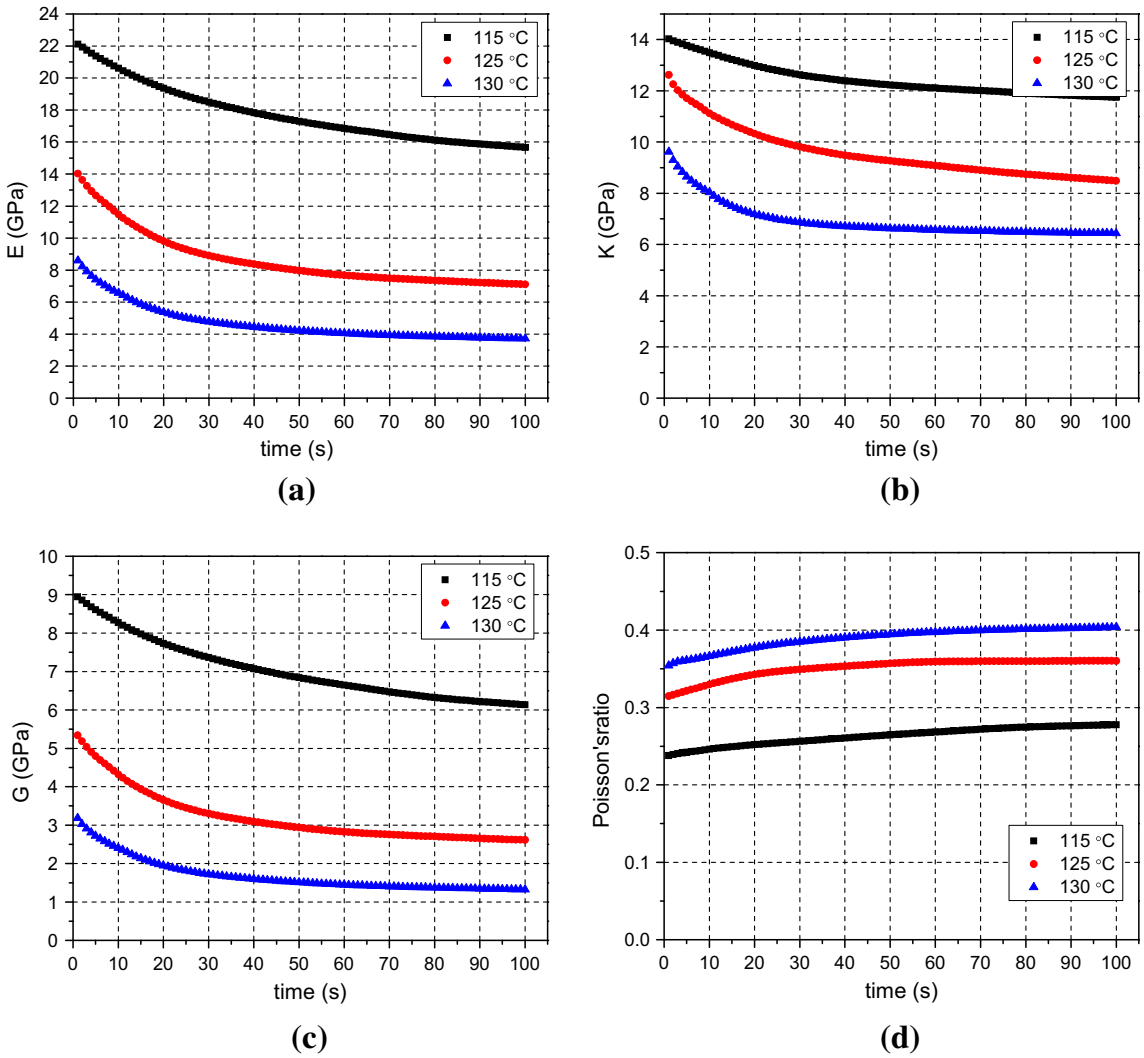

Fig. 14 Time-dependent properties at three temperatures in the glass transition range: **a** Young's modulus, **b** bulk modulus, **c** shear modulus and **d** Poisson's ratio

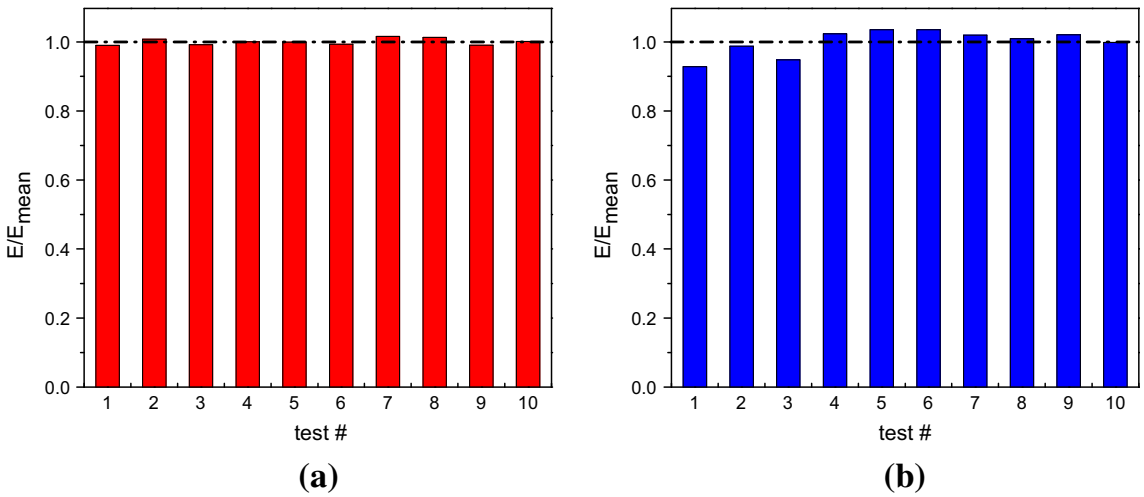

Fig. 15 Repeatability of uniaxial loading test at **a** 25 °C and **b** 175 °C

Supplementary testing was conducted to assess the measurement uncertainties of the uniaxial testing.

The uniaxial testing was repeated 10 times at 25 °C and 175 °C. The mean and standard deviation of Young's modulus were 29.13 GPa and 0.26 GPa at 25 °C and 1.59 GPa and 0.05 GPa at 175 °C, respectively. The data normalized by the mean values are shown in Fig. 15. The standard deviations are 0.89 % (25 °C) and 3.18 % (175 °C) of the mean values. The larger uncertainties at the higher temperature is attributed to the smaller load used in the test. A cylinder with low friction and higher pressure loading can be employed to further reduce the uncertainty.

Conclusion

A complete set of the elastic properties of an advanced EMC material was measured as a function of temperature using the FBG sensor based method. The single specimen configuration was used for both compressive and hydrostatic testing to measure two different elastic constants. With a single configuration, the uncertainties associated with specimen-to-specimen variations were completely eliminated. The proposed method is ideally suited to temperature and time -dependent polymer properties. The specimen with the embedded FBG sensor can be further utilized to study the environmental degradation of EMC materials.

Appendix

Substituting Eq. (2) into Eq. (6) yields:

$$\Delta\lambda = \frac{1}{E_f}\left\{\left[1-\frac{n^2}{2}\left(P_{12}-(P_{12}+P_{11})\nu_f\right)\right]\left[\frac{2E_f\nu_f C_{1f}}{(1+\nu_f)(1-2\nu_f)}+\frac{2E_f\nu_f{}^2 c}{(1+\nu_f)(1-2\nu_f)}+E_f c\right]\right.$$
$$\left.-\left[2\nu_f+\frac{n^2}{2}\left((1-\nu_f)P_{11}+(1-3\nu_f)P_{12}\right)\right]\left[\frac{E_f}{1+\nu_f}\left[\frac{C_{1f}}{1-2\nu_f}-\frac{C_{2f}}{r^2}\right]+\frac{E_f\nu_f c}{(1+\nu_f)(1-2\nu_f)}\right]\right\}\lambda_i \tag{A.1}$$

Next, substituting Eq. (4) into Eq. (A.1) yields:

$$\Delta\lambda = \frac{1}{E_f}\left\{\left[1-\frac{n^2}{2}\left(P_{12}-(P_{12}+P_{11})\nu_f\right)\right]\left[\frac{2E_f\nu_f}{(1+\nu_f)(1-2\nu_f)}\left(\frac{CE-BF}{AE-BD}+\left(\frac{1}{(1-2\nu_p)(1+\nu_p)}\frac{CE-BF}{AE-BD}\right.\right.\right.\right.$$
$$\left.\left.\left.\left.+\frac{\nu_p}{(1-2\nu_p)(1+\nu_p)}\frac{CD-AF}{BD-AE}-\frac{P_1}{E_p}\right)(1+\nu_p)\right)+\frac{2E_f\nu_f{}^2}{(1+\nu_f)(1-2\nu_f)}\frac{CD-AF}{BD-AE}+E_f\frac{CD-AF}{BD-AE}\right]\right.$$
$$\left.-\left[2\nu_f+\frac{n^2}{2}\left((1-\nu_f)P_{11}+(1-3\nu_f)P_{12}\right)\right]\left[\frac{E_f}{1+\nu_f}\left(\frac{1}{1-2\nu_f}\left(\frac{CE-BF}{AE-BD}+\left(\frac{1}{(1-2\nu_p)(1+\nu_p)}\frac{CE-BF}{AE-BD}\right.\right.\right.\right.\right.$$
$$\left.\left.\left.\left.\left.+\frac{\nu_p}{(1-2\nu_p)(1+\nu_p)}\frac{CD-AF}{BD-AE}-\frac{P_1}{E_p}\right)(1+\nu_p)\right)\right)+\frac{E_f\nu_f}{(1+\nu_f)(1-2\nu_f)}\frac{CD-AF}{BD-AE}\right]\right\}\lambda_i \tag{A.2}$$

Finally, the governing equation can be obtained by substituting Eq. (5) into Eq. (A.2).

Reference

1. Kelly G, Lyden C, Lawton W, Barrett J, Saboui A, Pape H, Peters HJ (1996) Importance of molding compound chemical shrinkage in the stress and warpage analysis of PQFPs. Components Packag Manuf Technol B IEEE Trans Adv Packag 19:296–300
2. Kong JW, Kim J-K, Yuen MM (2003) Warpage in plastic packages: effects of process conditions, geometry and materials. IEEE Trans Electron Packag Manuf 26:245–252
3. Ernst L, Zhang G, Jansen K, Bressers H (2003) Time-and temperature-dependent thermo-mechanical modeling of a packaging molding compound and its effect on packaging process stresses. J Electron Packag 125:539–548
4. O'Brien DJ, Sottos N, White SR (2007) Cure-dependent viscoelastic Poisson's ratio of epoxy. Exp Mech 47:237–249
5. Van Driel W, Janssen J, Zhang G, Yang D, Ernst L (2003) Packaging induced die stresses—effect of chip anisotropy and

time-dependent behavior of a molding compound. J Electron Packag 125:520–526
6. Tschoegl NW, Knauss WG, Emri I (2002) Poisson's ratio in linear viscoelasticity–a critical review. Mech Time-Dependent Mater 6:3–51
7. Sadeghinia M, Jansen K, Ernst L (2012) Characterization and modeling the thermo-mechanical cure-dependent properties of epoxy molding compound. Int J Adhes Adhes 32:82–88
8. Emri I, Prodan T (2006) A measuring system for bulk and shear characterization of polymers. Exp Mech 46:429–439
9. Wang Y, Woodworth L, Han B (2011) Simultaneous measurement of effective chemical shrinkage and modulus evolutions during polymerization. Exp Mech 51:1155–1169
10. Sun Y, Wang Y, Jang C, Han B, Choi K (2013) Generalized hybrid modeling to determine chemical shrinkage and modulus evolutions at arbitrary temperatures. Exp Mech 53:1783–1790
11. Sun Y, Wang Y, Kim Y, Han B (2014) Dual-configuration fiber Bragg grating sensor technique to measure coefficients of thermal expansion and hygroscopic swelling. Exp Mech 54:593–603
12. Sun Y, Han B, Parsa E, Dasgupta A (2014) Measurement of effective chemical shrinkage and equilibrium modulus of silicone elastomer used in potted electronic system. J Mater Sci 49:8301–8310
13. Karalekas D, Cugnoni J, Botsis J (2008) Monitoring of process induced strains in a single fibre composite using FBG sensor: a methodological study. Compos A: Appl Sci Manuf 39:1118–1127
14. Tanaka N, Okabe Y, Takeda N (2003) Temperature-compensated strain measurement using fiber Bragg grating sensors embedded in composite laminates. Smart Mater Struct 12:940
15. Tao X, Tang L, Du W-c, Choy C-l (2000) Internal strain measurement by fiber Bragg grating sensors in textile composites. Compos Sci Technol 60:657–669
16. Prigogine I (1967) Introduction to thermodynamics of irreversible processes. New York: Interscience, 3rd ed., vol. 1, 1967
17. Procter P and Solc J (1991) Improved thermal conductivity in microelectronic encapsulants. In: Electronic Components and Technology Conference, Proceedings., 41st, pp. 835–842
18. Brinson HF and Brinson LC (2008) Polymer engineering science and viscoelasticity: Springer
19. Blankleider B, Woloshyn R (1984) Quasi-elastic scattering of polarized electrons on polarized He 3. Phys Rev C 29:538
20. Brenner R, Masson R, Castelnau O, Zaoui A (2002) A "quasi-elastic" affine formulation for the homogenised behaviour of nonlinear viscoelastic polycrystals and composites. Eur J Mech-A/Solids 21:943–960